Framework-Porphyrin-Derived Single-Atom Bifunctional Oxygen Electrocatalysts and their Applications in Zn–Air Batteries

Bo-Quan Li, Chang-Xin Zhao, Shuangming Chen, Jia-Ning Liu, Xiao Chen, Li Song, and Qiang Zhang*

High-performance bifunctional oxygen electrocatalysis constitutes the key technique for the widespread application of clean and sustainable energy through electrochemical devices such as rechargeable Zn–air batteries. Single-atom electrocatalysts with maximum atom efficiency are highly considered as an alternative of the present noble-metal-based electrocatalysts. However, the fabrication of transition metal single-atoms is very challenging, requiring extensive attempts of precursors with novel design principles. Herein, an all-covalently constructed cobalt-coordinated framework porphyrin with graphene hybridization is innovatively designed and prepared as the pyrolysis precursor to fabricate single-atom Co–N_x–C electrocatalysts. Excellent electrochemical performances are realized for both bifunctional oxygen electrocatalysis and rechargeable Zn–air batteries with regard to reduced overpotentials, improved kinetics, and prolonged cycling stability comparable with noble-metal-based electrocatalysts. Design principles from multiple scales are proposed and rationalized with detailed mechanism investigation. This work not only provides a novel precursor for the fabrication of high-performance single-atom electrocatalysts, but also inspires further attempts to develop advanced materials and emerging applications.

The ever growing global energy consumption demands sustainable energy supply.[1] Fuel cells, metal–air batteries, and water splitting devices are highly regarded as desirable next-generation energy storage or conversion techniques.[2] Among them, rechargeable aqueous Zn–air batteries attract increasing attentions because of their high energy density of 1086 Wh kg^{-1} (including oxygen), low cost, environmental friendliness, and

B.-Q. Li, C.-X. Zhao, J.-N. Liu, Dr. X. Chen, Prof. Q. Zhang
Beijing Key Laboratory of Green Chemical Reaction Engineering and Technology
Department of Chemical Engineering
Tsinghua University
Beijing 100084, P. R. China
E-mail: zhang-qiang@mails.tsinghua.edu.cn
Dr. S. Chen, Prof. L. Song
National Synchrotron Radiation Laboratory
CAS Center for Excellence in Nanoscience
University of Science and Technology of China
Hefei, Anhui 230029, P. R. China

The ORCID identification number(s) for the author(s) of this article can be found under https://doi.org/10.1002/adma.201900592.

intrinsic safety.[3] However, the cathode oxygen redox reactions, referring to the oxygen reduction reaction (ORR) and the oxygen evolution reaction (OER), are highly sluggish in kinetics and considerably limit the practical performance of not only rechargeable Zn–air batteries, but also the above-mentioned techniques.[4] Therefore, developing high-performance bifunctional oxygen electrocatalysts for both ORR and OER is of great significance to using clean energy through sustainable pathways.[5]

Tremendous efforts have been made in searching for high-performance bifunctional oxygen electrocatalysts in the past decades. Noble-metal-based electrocatalysts exhibit ideal reactivity and serve as the benchmark (for instance, Pt/C for ORR and Ir/C for OER).[6] Unfortunately, the high cost and earth scarcity limit their large-scale applications.[7] Noble-metal-free electrocatalysts, including nanocarbon,[8] layered double hydroxides,[9] perovskites,[10] sulfides,[11] nitrides,[12] and their composites[13] are intensively investigated. Heteroatom doping,[14] defect engineering,[15] and ionic regulation[16] serve as effective strategies to optimize the electrocatalytic performance. Nevertheless, the pursuit for high intrinsic reactivity and maximum utilization of the active sites has never come to an end.

Very recently, single-atom catalysts (SACs) are proposed as a new material family for heterogeneous catalysis.[17] Since the first report by Zhang and co-workers,[18] a number of SACs were fabricated and demonstrate distinctive catalytic behaviors for various reactions.[19] Particularly, single-atom M–N–C electrocatalysts (where M is a transition metal atom) affords extraordinary electrocatalytic performances because of the advantages including ultrahigh intrinsic reactivity, maximum atom efficiency, and favorable electronic conduction and ion transport endowed by the carbon skeleton.[20] For instance, single-atom nickel in graphene manifests sufficient electrochemical hydrogen production reactivity,[21] NiN_4C_4 moieties provide high OER performance,[22] and single-atom iron anchored nitrogen-doped carbon exhibits desirable ORR performance with reduced overpotential compared with Pt/C electrocatalysts.[23] Therefore, the unique single-atom M–N–C

materials constitute the frontiers in regards of advanced synthesis, characterization, and electrocatalysis investigation.

Despite the advantages of SACs, their fabrication remains a great challenge. A common approach to obtain single-atom M–N–C materials is through pyrolysis of the corresponding precursors with carbon, nitrogen, and transition metal contents.[24] It is conceivable that the structure and composition of the precursors have great influence on the properties of the products. Metal-containing carbon matrix[25] and metal–organic frameworks[26] serve as the pyrolysis precursors in most cases. However, the conversion from the precursor to the desired single-atom M–N–C materials requires delicate synthetic procedures in regards of precise precursor fabrication and well-controlled pyrolysis conditions, hindering the widespread application of SACs. Therefore, further efforts to enrich the precursors for single-atom M–N–C materials are strongly considered with detailed investigation in precursor selection. Additionally, the majority of the single-atom M–N–C electrocatalysts merely afford single-function for either ORR or OER, which cannot satisfy practical applications in rechargeable Zn–air batteries. Developing bifunctional single-atom M–N–C electrocatalysts for both ORR and OER is of higher value to motivate the evolution in clean and sustainable energy.

As an emerging carbon-based material, all-covalently constructed organic framework materials demonstrate potential advances serving as precursors for single-atom M–N–C materials. The directivity and saturability of covalent bonds guarantee the well-defined structure of organic frameworks.[27] Correspondingly, predesign and precise synthesis can be simultaneously achieved according to reticular chemistry.[28] More importantly, the framework skeleton explicitly constructed by covalent bonds is independent from metal-involved coordination interactions, providing more space for structural design of the precursor. Nevertheless, the synthesis of organic framework materials is complicated with limited yield and output.[29] In addition, most organic frameworks are 2D and exhibit the structure of eclipsed AA stacking. Compact arrangement of the metal contents inevitably results in metal aggregation to render serious loss of desired single-atom sites during pyrolysis.[30]

In this contribution, a hybrid of cobalt-coordinated framework porphyrin with graphene (named as Co-G@POF) was designed and prepared as the pyrolysis precursor to fabricate single-atom Co–N_x–C electrocatalysts for bifunctional oxygen electrocatalysis and Zn–air battery applications. The cobalt-coordinated framework porphyrin (Co-POF) was selected based on the consideration of its analogue molecular structure as Co–N_x–C moieties and facile one-pot synthesis with high yield and output,[31] where cobalt demonstrates high reactivity for bifunctional oxygen electrocatalysis.[32] On the other hand, graphene (named as G) serves as the template for morphology regulation of framework porphyrin from stacking. The pyrolyzed product derived from Co-G@POF (named as Co-POC) possesses desired single-atom Co–N_x–C structures validated by comprehensive characterizations. The Co-POC electrocatalyst demonstrates excellent bifunctional oxygen electrocatalytic performances with a small overpotential gap of 0.87 V comparable with noble-metal-based electrocatalysts, rapid kinetics with reduced Tafel slopes, and long-term durability. Consequently, rechargeable Zn–air batteries using the Co-POC cathode afford higher power density, improved rate performance, and cycling stability for over 200 cycles at 2.0 mA cm^{-2} beyond the noble-metal-based cathode.

Figure S1 (Supporting Information) demonstrates the fabrication of Co-POC that involves one-pot synthesis and following pyrolysis of the Co-G@POF precursor. The content of the cobalt-coordinated framework porphyrin was designed to be 20 wt% in Co-G@POF with a theoretical cobalt content of 22.9 mg g^{-1}. Fourier transformed infrared spectrometry (FTIR) was first performed to evaluated the construction of framework porphyrin. The adsorption peak of G at 1550 cm^{-1} is assigned to typical C=C vibration (Figure S2, Supporting Information). In comparison, Co-G@POF affords an adsorption peak at higher wavenumber of 1650 cm^{-1}, which is attributed to the C=N vibration of porphyrin.[33] X-ray diffraction (XRD) patterns of Co-G@POF exhibit a distinguished peak of framework porphyrin at 13° from G with two ordinary diffraction peaks at around 26° and 42°,[34] indicating the intrinsically ordered structure different from amorphous polymers (Figure S3, Supporting Information).[35] Elemental analysis was carried out using comprehensive methods including X-ray photoelectron spectroscopy (XPS), energy-dispersive X-ray spectrometry (EDS), and inductively coupled plasma optical emission spectrometry (ICP). Both XPS and EDS results manifest an increase in nitrogen and cobalt contents compared with G (Figures S4 and S5, Supporting Information). For instance, the nitrogen and cobalt contents are 3.6 and 0.4 at% for Co-G@POF and 0.4 and 0.0 at% for G, respectively. Further ICP analysis confirms the cobalt content of 24.8 mg g^{-1} in agreement with the theoretical value (Table S1, Supporting Information). High-resolution nitrogen 1s XPS spectrum demonstrates two deconvoluted peaks of pyrrolic N at 400.1 eV and Co–N at 398.5 eV, implying the cobalt content is coordinated within the porphyrin units (Figure S6, Supporting Information).[25] The above characterizations evidently prove successful fabrication of Co-G@POF suitable as the pyrolysis precursor for SACs (Tables S2 and S3, Supporting Information).

The morphology of the samples was characterized using a scanning electron microscope (SEM) and a transmission electron microscope (TEM). Compared with bare G (Figure S7, Supporting Information), Co-G@POF exhibits resemble morphology of G sheets without any heterogeneous components (Figure S8, Supporting Information). The uniform morphology of Co-G@POF suggests that framework porphyrin is dominantly hybridized with G instead of stacking into aggregated particles, which is attributed to the strong intermolecular π–π interactions between Co-POF and G. The pore structure was evaluated using nitrogen isothermal sorption measurements. Co-G@POF affords a specific surface area of 581.3 m^2 g^{-1} and pore volume of 1.74 cm^3 g^{-1}, respectively (Figure S9, Supporting Information). The characteristic micropore structure of Co-G@POF at 1.4 nm is identified as the intrinsic pore of framework porphyrin.

Co-G@POF features cobalt-coordinated porphyrin covalently linked into 2D framework that is hybridized on the surface of G through intermolecular π–π interactions. This structure is highly considered as the precursor to fabricated SACs. Single-atom Co-POC was fabricated by pyrolysis at 950 °C under argon and hydrogen atmosphere followed by acid etching to remove
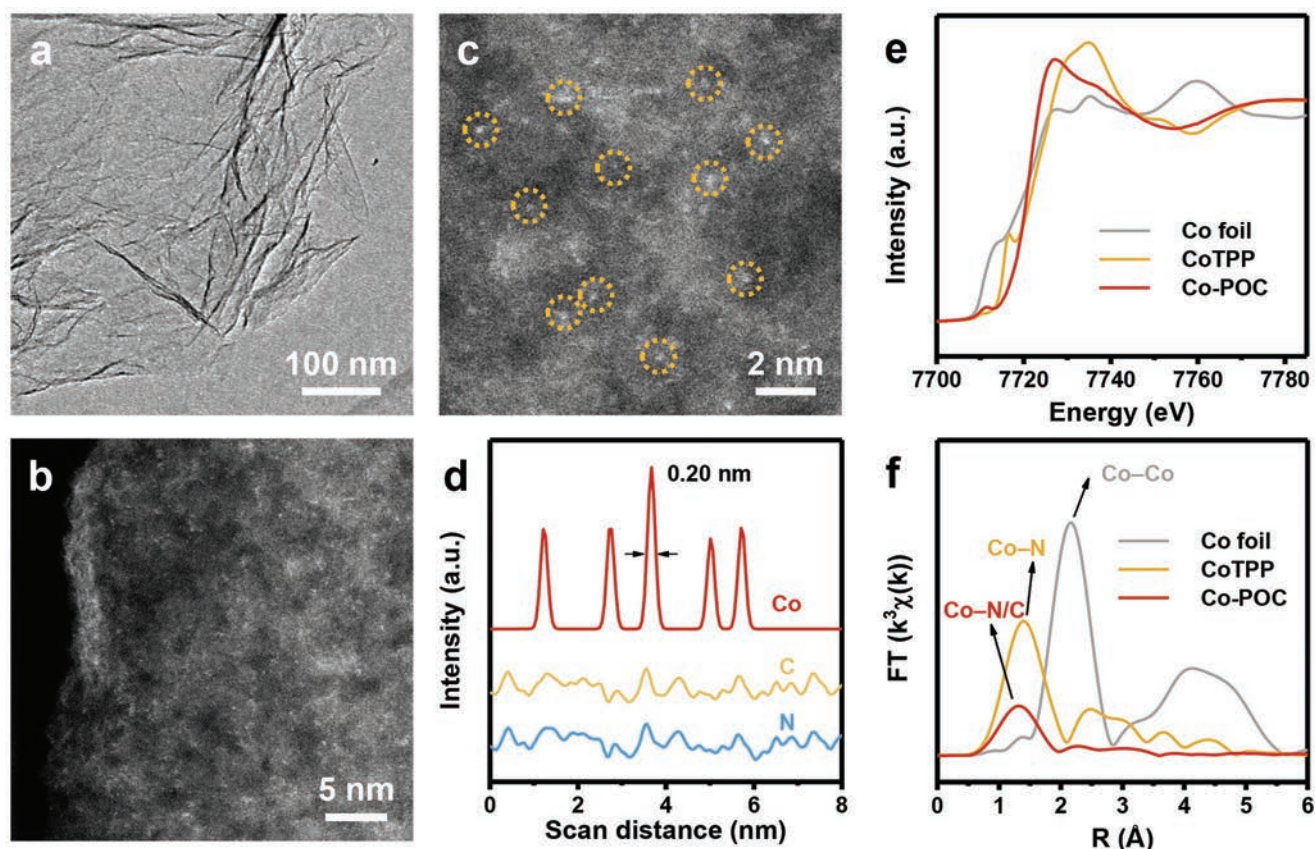
Figure 1. Single-atom characterization of Co-POC. a) TEM image of Co-POC. b) HADDF-STEM image and c) corresponding enlarged view of Co-POC. The bright dots highlighted with yellow circles in (c) marks the cobalt single-atoms in Co-POC. d) Line-scan analysis of carbon, nitrogen, and cobalt based on EDS mapping. e) XANES spectra and f) Fourier-transformed EXAFS spectra at the Co K-edge of cobalt foil, CoTPP, and Co-POC.

undesired cobalt nanoparticles. Elemental analysis indicates a decrease in nitrogen and cobalt contents (Figures S10 and S11, Supporting Information). Nevertheless, the cobalt content remains 0.2 at% by XPS and 15.4 mg g^{-1} by ICP, respectively, suggesting that partial cobalt content was maintained within the carbon skeleton. SEM and TEM images of Co-POF afford a uniform contrast without any aggregated cobalt component (**Figure 1**a; Figure S12, Supporting Information). Further XRD characterization confirms the absence of metallic cobalt or any other cobalt compound, implying that the remained cobalt content is isolated rather than aggregated to form cobalt nanoparticles (Figure S13, Supporting Information). Besides, pore structure analysis exhibits slightly increased specific surface area and pore volume of Co-POC compared with Co-G@POF (Figure S14, Supporting Information). Accordingly, the carbon skeleton is suggested to be stable during pyrolysis.

Aberration-corrected high-angel annular dark field scanning transmission electron microscopy (HADDF-STEM) with ultrahigh resolution was applied to identify single-atom cobalt within the carbon skeleton. Isolated cobalt single-atoms are unambiguously observed as the bright dots, which is highlighted by yellow circles (Figure 1b,c). EDS elemental mapping was further performed under the STEM mode, which demonstrates uniform distribution of carbon, nitrogen, and cobalt (Figure S15, Supporting Information). Line-scan analysis across

the arrow affords continuous signals for carbon and nitrogen contrast but exclusively isolated signals for cobalt (Figure 1d). The full width at half maxima of the cobalt spectrum is 0.20 nm, which matches the diameter of cobalt single atoms.

X-ray absorption spectroscopy is a powerful technique to characterize the single-atom structure and the coordination environment of the center single-atom. Metallic cobalt foil and 5, 10, 15, 20-tetrakis(4-methoxyphenyl)porphyrinato cobalt (CoTPP) served as the reference samples with defined Co–Co and Co–N interactions, respectively. X-ray absorption near-edge structure (XANES) spectra exhibit a pre-edge peak at 7711 eV of Co-POC ascribed as the fingerprint of single-atom Co–N$_x$–C structures (Figure 1e).[36] Fourier-transformed (FT) extended X-ray absorption fine structure (EXAFS) spectrum of Co-POC demonstrates only one peak at 1.32 Å identified as the Co–N/C first coordination shell (Figure 1f), which is in agreement with the Co–N peak at 1.38 Å of the reference CoTPP sample.[37] No Co–Co interaction at 2.16 Å or other high-shell peak is observed, indicating that cobalt atoms are isolated through coordination with surrounding nitrogen/carbon atoms into single-atom Co–N$_x$–C structures without metallic cobalt or cobalt compounds. EXAFS fitting was further performed for quantitative analysis of the single-atom Co–N$_x$–C structures of Co-POC. The EXAFS fitting parameters and fitting curves are demonstrated in Table S4 and Figure S16 (Supporting Information), respectively. The

coordination number of Co-POC is fitted to be 3.5±2 with a simulated Co–N bond length of 1.89±0.02 Å. The simulated results match well with CoTPP but differ from Co foil, further indicating the single-atom Co–N$_x$–C structures of Co-POC. In addition, high-resolution nitrogen 1s XPS spectrum affords Co–N interactions at 398.5 eV to serve as a side evidence of the XAS results (Figure S17, Supporting Information). Therefore, Co-POC is evidently proved to exclusively possess single-atom cobalt qualified as SACs.

Electrochemical evaluation was carried out to probe the bifunctional oxygen electrocatalytic performance of Co-POC as a single-atom electrocatalyst. Commercial 20% Pt/C and 20% Ir/C were selected as the benchmark ORR and OER electrocatalysts, respectively, with an areal loading for all electrocatalysts being 0.10 mg cm^{-2}. All electrochemical measurements were performed in oxygen-saturated 0.10 M KOH aqueous electrolyte at room temperature.

The ORR reactivity was evaluated using linear sweep voltammetry (LSV). The Co-POC electrocatalyst demonstrates an ORR half-wave potential ($E_{1/2}$) of 0.83 V versus reversible hydrogen electrode (RHE) (**Figure 2**a), which is very close to the Pt/C electrocatalyst of 0.85 V versus RHE and much better than G. The ORR LSV profiles are declining at high current densities for G and Co-POC because of the limitation of mass transportation. Tafel plots in Figure 2b manifest that the ORR kinetics is significantly improved on the Co-POC electrocatalyst (53.5 mV dec^{-1}) over Pt/C (88.6 mV dec^{-1}) and G (115 mV dec^{-1}). The ORR electron transfer number (n) characterize the pathway for oxygen reduction. The n value is 3.6 at 0.80 V versus RHE for

Co-POC and maintains stable within the ORR potential range (Figure S18, Supporting Information), implying the dominant four-electron ORR pathway similar as the Pt/C electrocatalyst. In contrast, G alone affords a mixed pathway with the ORR electron transfer number being around 3.0.

The durability of the electrocatalysts was evaluated according to the long-term chronoamperometric responses (Figure 2c). The Co-POC electrocatalyst affords 70% of the initial current density after 65 000 s while only 44% of the initial current density is remained after 40 000 s for Pt/C. Conclusively, single-atom Co-POC electrocatalyst exhibits ORR reactivity, kinetics, and stability comparable or superior than the state-of-the-art noble-metal-based Pt/C electrocatalyst.

The OER reactivity and kinetics are similarly evaluated according to LSV profiles and Tafel slopes but with Ir/C as the reference electrocatalyst. The OER overpotential required to reach the current density of 10 mA cm^{-2} (η_{10}) is selected as the descriptor for OER reactivity. The η_{10} is 470 mV for Co-POC and 410 mV for Ir/C, respectively, indicating inferior OER reactivity of the Co-POC electrocatalyst (Figure 2d). Nevertheless, Co-POC affords a reduced Tafel slope of 139 mV dec^{-1} compared with Ir/C of 173 mV dec^{-1} (Figure 2e). Comprehensively, the OER performance of Co-POC is acceptable considering the obvious improvement in comparison with G.

Bifunctional ORR/OER electrocatalytic performance is of great significance to practical Zn–air battery applications. The potential gap (ΔE) between the ORR half-wave potential and the OER potential at 10 mA cm^{-2} is widely accepted to evaluate the ORR/OER bifunctional performance.[38] The Co-POC electrocatalyst
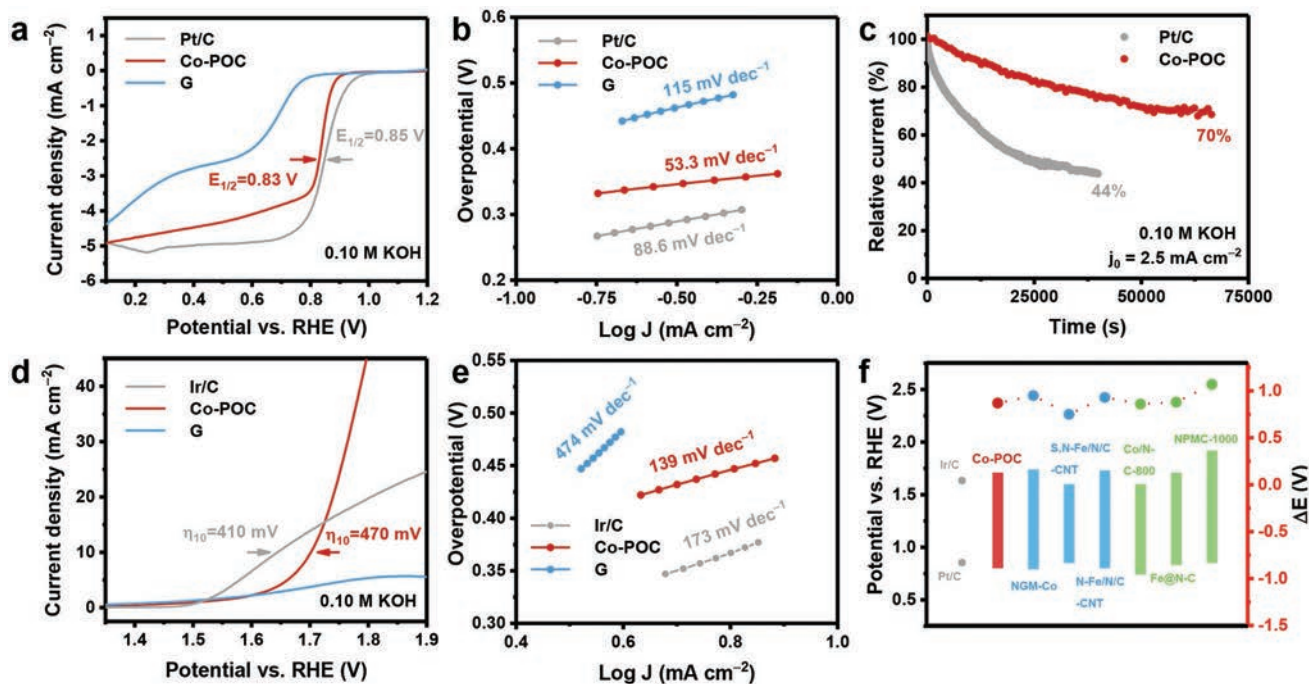

Figure 2. Bifunctional oxygen electrocatalytic performance evaluation of the single-atom Co-POC electrocatalyst. a) 95% *iR*-compensated ORR LSV profiles and b) corresponding Tafel plots of Pt/C, Co-POC, and G electrocatalysts. c) ORR durability evaluation of Pt/C and Co-POC electrocatalysts at a constant potential required to reach an initial current density of 2.5 mA cm^{-2}. d) 95% *iR*-compensated OER LSV profiles and e) corresponding Tafel plots of Ir/C, Co-POC, and G electrocatalysts. f) Comparison of ORR/OER bifunctional electrocatalytic performance of Pt/C-Ir/C, Co-POC, and other reported electrocatalysts.

affords a ΔE of 0.87 V, which is among the best noble-metal-free bifunctional oxygen electrocatalysts in previous reports (Figure 2f; Table S5, Supporting Information).[25,39] Therefore, the single-atom Co-POC electrocatalyst is demonstrated to possess excellent bifunctional ORR/OER electrocatalytic performance.

The successful fabrication of single-atom Co–N_x–C and desirable bifunctional ORR/OER electrocatalytic performance of Co-POC are highly dependent on the rational design of the Co-G@POF precursor. The predesigned cobalt-coordinated porphyrin units, the 2D framework porphyrin skeleton, and the hybridization with G templates are proposed to have great influences on the production of single-atom electrocatalysts and corresponding electrocatalytic performances. In order to validate the above proposition, further mechanism investigation was carried out by using pyrolysis precursors without porphyrin unit for cobalt coordination, the framework porphyrin skeleton, or the G templates for hybridization, respectively. Control samples were fabricated using the corresponding precursors following identical pyrolysis procedures and characterized and evaluated in regards of morphology, composition, and electrochemical performances.

The pyrolysis precursor without porphyrin units for cobalt coordination was fabricated by mixing G and cobalt nitride as the cobalt and nitrogen source, which is named as Co/G. Without porphyrin coordination to restrict the cobalt atoms, aggregated nanoparticles were observed in TEM images of Co/G (Figure S19, Supporting Information). As expected, cobalt nanoparticles were obtained unevenly distributed on the graphene surface after pyrolysis (Figure S20, Supporting Information). The exposed cobalt nanoparticles are unstable against acid. Not surprisingly, despite the reasonable cobalt content in the Co/G precursor (Figures S21 and S22, Supporting Information), the sample after pyrolysis and acid treatment (named as Co-G) affords a very limited cobalt content of 0.04 at% by ICP and 0.0 at% by XPS compared with Co-POC (**Figure 3**a), which was further confirmed by morphology characterization (Figure S23, Supporting Information). With a relative low cobalt content preserved, the Co-G electrocatalyst exhibits poor performance for both ORR and OER. The ORR $E_{1/2}$ decreases to 0.35 V versus RHE (Figure 3d) and the OER current density is below 10 mA cm^{-2} even at 1.9 V versus RHE (Figure 3e). Therefore, porphyrin coordination evidently contributes to preserve the cobalt content within the carbon skeleton from aggregation and acid etching.

The porphyrin units pre-distribute cobalt atoms through coordination. However, the cobalt-coordinated porphyrin small
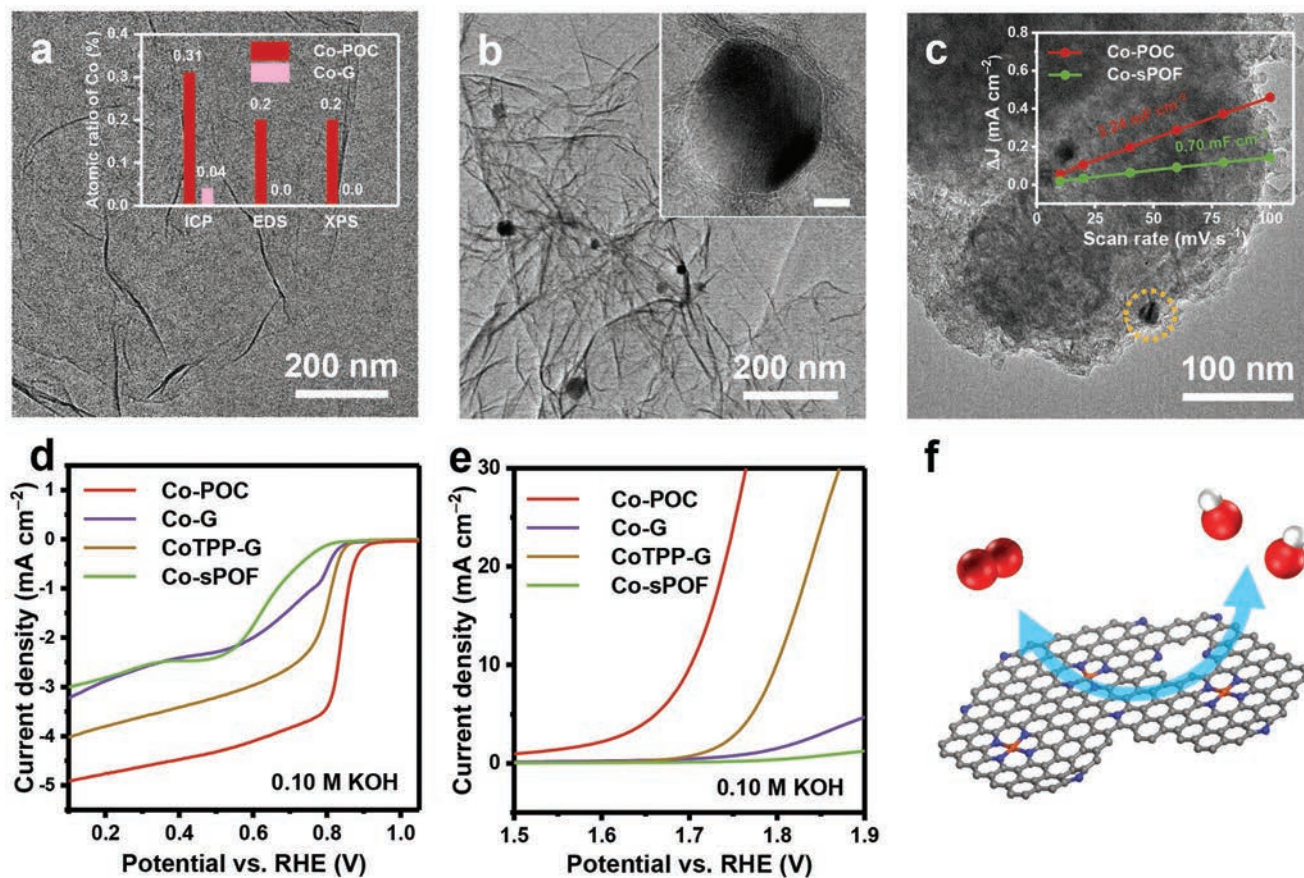

Figure 3. Investigation of the dependence of the electrocatalysts on the structure of the corresponding pyrolysis precursors. a) TEM image of Co-G. The inset (a) is the relative cobalt amount of Co-POC and Co-G. b) TEM image of CoTPP-G. The inset (b) is the enlarged view. The scale bar in the insert is 5 nm. c) TEM image of Co-sPOF. The inset (c) is the ECSA of Co-POC and Co-sPOF. d,e) 95% *iR*-compensated ORR (d) and OER (e) LSV profiles of Co-POC, Co-G, CoTPP-G, and Co-sPOF electrocatalysts. f) Scheme of bifunctional oxygen electrocatalysis on single-atom Co–N_x–C electrocatalysts. The hydrogen, carbon, nitrogen, oxygen, and cobalt atoms are marked with white, gray, blue, red, and orange, respectively.

**ADVANCED
SCIENCE NEWS**

www.advancedsciencenews.com

**ADVANCED
MATERIALS**

www.advmat.de

molecules tend to stack with each other if not covalently linked into framework skeleton. Consequently, aggregation of cobalt cannot be avoided during pyrolysis to render relative low content of single-atom Co–N_x–C and inferior ORR/OER performance. To prove the above hypothesis, CoTPP, a small molecule with defined structure of cobalt-coordinated porphyrin, was selected as the cobalt and nitrogen source and mixed with G to fabricated the pyrolysis precursor named as CoTPP/G as a verification. SEM and TEM images exhibit aggregated CoTPP on the graphene surface (Figure S24, Supporting Information). Due to the carbon/nitrogen-rich environment around the cobalt source, a unique morphology of cobalt nanoparticles enveloped by carbon layers was observed after pyrolysis (Figure S25, Supporting Information). The coating of the carbon layers protects the inner cobalt nanoparticles from acid etching. Accordingly, these cobalt nanoparticles are preserved after acid treatment (where the sample is named as CoTPP-G) (Figure 3b; Figure S26, Supporting Information). Although the cobalt content of CoTPP-G is close to Co-POC (0.2 at% by XPS) (Figures S27 and S28, Supporting Information), most of the cobalt content is aggregated in nanoparticles instead of isolated cobalt single-atoms.

When employing CoTPP-G as the bifunctional oxygen electrocatalyst, the ORR $E_{1/2}$ is 0.72 V versus RHE (Figure 3d) and the OER η_{10} is 570 mV (Figure 3e), neither of which is comparable with the Co-POC electrocatalyst. Interestingly, CoTPP-G affords similar ORR and OER Tafel slopes as Co-POC, which is suggested to be attributed by partial isolated cobalt contents in the coating carbon layer (Figure S29, Supporting Information). Nevertheless, the enveloped cobalt nanoparticles are undesirable as active sites for bifunctional oxygen electrocatalysis (ΔE = 1.08 V) compared with Co-POC (ΔE = 0.87 V), further verifying the necessity of the framework structure that covalently links the porphyrin units into 2D skeleton for sufficient fabrication of single-atom Co–N_x–C electrocatalysts.

Even the well-defined cobalt-coordinated porphyrin units are covalently linked into skeleton, the 2D nature of the framework porphyrin makes itself easy to stack into dense spheres without the hybridization of graphene templates (Figure S30, Supporting Information). Although the cobalt atoms and porphyrin units are pre-dispersed, the pyrolysis precursor without graphene hybridization (named as Co/sPOF) inevitably results in aggregated cobalt nanoparticles after pyrolysis (Figure S31, Supporting Information), which are preserved in the final product (named as Co-sPOF) (Figure 3c; Figure S32, Supporting Information). More importantly, the dense morphology of Co/sPOF renders reduced electrochemical surface area (ECSA) (Figure 3c, inserted) of Co-sPOF, which is disadvantageous for oxygen electrocatalysis. Even with higher cobalt content than Co-POC (Figures S33 and S34, Supporting Information), the Co-sPOF electrocatalyst affords very poor oxygen electrocatalytic performance with limited ORR and OER current density far from satisfaction. Based on the above discussion, we come to the conclusion that the cobalt-coordinated porphyrin units, the 2D framework porphyrin skeleton, and the hybridization with G templates constitute three main factors for covalently constructed organic frameworks as pyrolysis precursors to fabricate high-performance single-atom bifunctional oxygen electrocatalysts.

The successful construction of single-atom Co–N_x–C and excellent bifunctional oxygen electrocatalytic performance of Co-POC promise further application in Zn–air batteries. A conventional rechargeable Zn–air battery is composed of a zinc foil as the anode, alkaline aqueous electrolyte that contains zinc salt, and an air cathode where the oxygen redox reactions take place (**Figure 4**a).[40] The cathode reactions constitute the
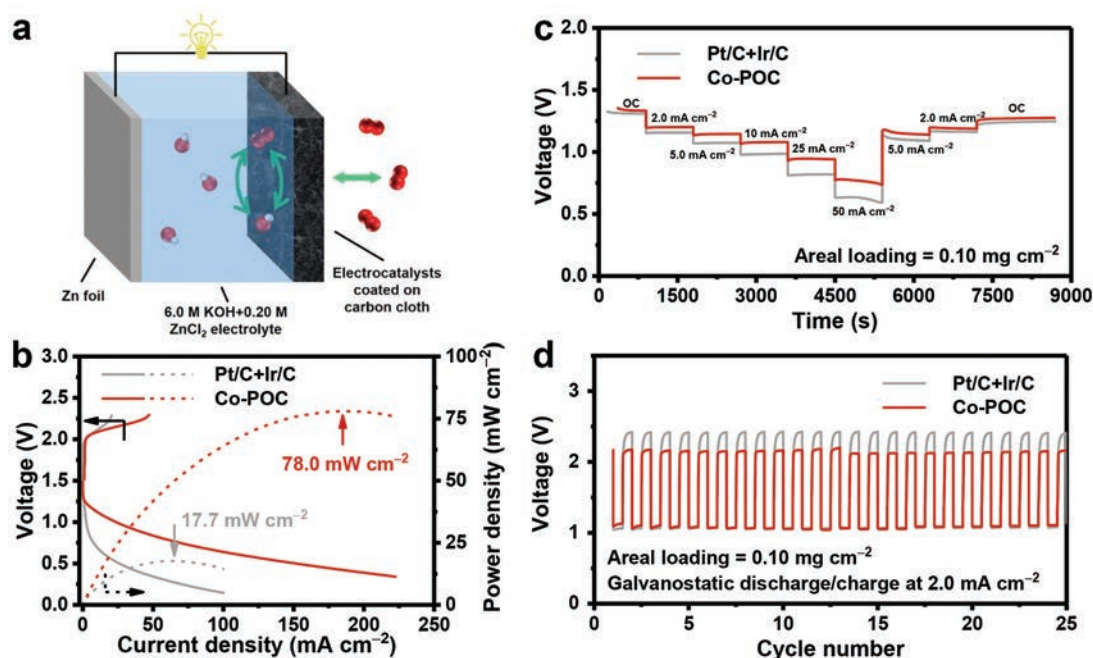

Figure 4. Electrochemical evaluation of the single-atom Co-POC-based cathode in rechargeable Zn–air batteries. a) Scheme of a conventional rechargeable Zn–air battery. b) LSV profiles, c) rate performance, and d) cycling stability at a discharge/charge current density of 2.0 mA cm^{-2} of the Co-POC and the Pt/C+Ir/C cathodes.

**ADVANCED
SCIENCE NEWS**

www.advancedsciencenews.com

**ADVANCED
MATERIALS**

www.advmat.de

bottleneck of Zn–air batteries because of sluggish kinetics of both ORR and OER. Therefore, the single-atom Co-POC electrocatalyst were loaded on conductive carbon cloth to construct the air cathode for better battery performance. Noble-metal-based Pt/C+Ir/C cathode was also prepared following similar procedures as Co-POC as the reference cathode.[41] The areal loading is 0.10 mg cm^{-2} for both of the electrocatalysts.

LSV was first performed to evaluate the reactivity of the cathode reactions. The Co-POC cathode exhibits discharge voltages of 1.12 and 1.03 V at the current density of 10 and 20 mA cm^{-2}, respectively, which are much higher than the Pt/C+Ir/C cathode (Figure 4b). Correspondingly, a peak discharge power density of 78.0 mW cm^{-2} is achieved on the Co-POC cathode while reduces to 17.7 mW cm^{-2} for the Pt/C+Ir/C cathode. Notably, the superior electrochemical performances of the Co-POC cathode than the Pt/C+Ir/C cathode are different from RRDE results, which is attributed to various testing conditions and methods between using RRED and in working Zn–air batteries. The rate performance was evaluated by discharging at different current densities. The Co-POC cathode demonstrates higher discharge voltages than the Pt/C+Ir/C cathode in all the cases (Figure 4c) with the voltage retention of 97.9% and 99.1% at 2.0 and 5.0 mA cm^{-2}, respectively. Superior rate performance of the Co-POC cathode suggests improved ORR kinetics and electrocatalytic capability in agreement with the LSV results.

The stability of the cathodes was characterized using long-term cycling tests. The Co-POC cathode exhibits an initial discharge/charge voltage gap of 1.04 V at 2.0 mA cm^{-2}, which is much reduced than the Pt/C+Ir/C cathode of 1.34 V (Figure 4d). The Co-POC cathode affords 237 cycles corresponding to 79 h (Figure S35, Supporting Information). At higher discharge/charge current density of 5.0 mA cm^{-2}, the Co-POC cathode stood for 164 cycles corresponding to 55 h while the Pt/C+Ir/C cathode failed at the 105 cycle (Figure S36, Supporting Information). Therefore, the single-atom Co-POC cathode with excellent bifunctional oxygen electrocatalytic performance demonstrates promising reactivity and stability in Zn–air batteries and highlights further applications of single-atom electrocatalysts in Zn–air batteries.

In conclusion, an all-covalently constructed Co-G@POF precursor was proposed to fabricate single-atom Co–N$_x$–C materials for bifunctional oxygen electrocatalysis and rechargeable Zn–air battery applications. The well-defined porphyrin units for cobalt coordination, the 2D framework porphyrin skeleton constructed by covalent bonds, and hybridization with graphene templates are highlighted as three key factors to realize isolated cobalt single-atoms in carbon skeleton. The as-synthesized single-atom Co-POC electrocatalyst demonstrates excellent bifunctional ORR/OER electrocatalytic performance with reduced overpotentials and improved kinetics. The rechargeable Zn–air batteries with the single-atom Co-POC electrocatalyst afford high peak power density of 78.0 mW cm^{-2}, reduced discharge/charge voltage gap of 1.04 V, and satisfactory stability of over 200 cycles at 2.0 mA cm^{-2} superior than the noble-metal-based electrocatalysts. This contribution not only provides sufficient bifunctional oxygen electrocatalysts with potential practical prospects, but also presents principles of rational design of precursors for fabrication of single-atom electrocatalysts.

Conflict of Interest

The authors declare no conflict of interest.

[1] S. Chu, Y. Cui, N. Liu, *Nat. Mater.* **2017**, *16*, 16.

[2] a) V. R. Stamenkovic, D. Strmcnik, P. P. Lopes, N. M. Markovic, *Nat. Mater.* **2017**, *16*, 57; b) F. Hu, S. Zhu, S. Chen, Y. Li, L. Ma, T. Wu, Y. Zhang, C. Wang, C. Liu, X. Yang, L. Song, X. Yang, Y. Xiong, *Adv. Mater.* **2017**, *29*, 1606570.

[3] a) Y. Li, H. Dai, *Chem. Soc. Rev.* **2014**, *43*, 5257; b) G. He, X. Han, B. Moss, Z. Weng, S. Gadipelli, F. Lai, A. G. Kafizas, D. J. L. Brett, Z. X. Guo, H. Wang, I. P. Parkin, *Energy Storage Mater.* **2018**, *15*, 380; c) H.-F. Wang, C. Tang, Q. Zhang, *Adv. Funct. Mater.* **2018**, *28*, 1803329.

[4] Y. Jiao, Y. Zheng, M. Jaroniec, S. Z. Qiao, *Chem. Soc. Rev.* **2015**, *44*, 2060.

[5] a) Z.-F. Huang, J. Wang, Y. Peng, C.-Y. Jung, A. Fisher, X. Wang, *Adv. Energy Mater.* **2017**, *7*, 1700544; b) D. Yang, L. Zhang, X. Yan, X. Yao, *Small Methods* **2017**, *1*, 1700209; c) Y. Lin, L. Yang, Y. Zhang, H. Jiang, Z. Xiao, C. Wu, G. Zhang, J. Jiang, L. Song, *Adv. Energy Mater.* **2018**, *8*, 1703623.

[6] M. Luo, Y. Sun, X. Zhang, Y. Qin, M. Li, Y. Li, C. Li, Y. Yang, L. Wang, P. Gao, G. Lu, S. Guo, *Adv. Mater.* **2018**, *30*, 1705515.

[7] Y. Lee, J. Suntivich, K. J. May, E. E. Perry, Y. Shao-Horn, *J. Phys. Chem. Lett.* **2012**, *3*, 399.

[8] J. Yang, H. Sun, H. Liang, H. Ji, L. Song, C. Gao, H. Xu, *Adv. Mater.* **2016**, *28*, 4606.

[9] C. Tang, H.-S. Wang, H.-F. Wang, Q. Zhang, G.-L. Tian, J.-Q. Nie, F. Wei, *Adv. Mater.* **2015**, *27*, 4516.

[10] X. Xu, W. Wang, W. Zhou, Z. Shao, *Small Methods* **2018**, *2*, 1800071.

[11] J. Zhang, T. Wang, D. Pohl, B. Rellinghaus, R. Dong, S. Liu, X. Zhuang, X. Feng, *Angew. Chem., Int. Ed.* **2016**, *55*, 6702.

[12] X. Jia, Y. Zhao, G. Chen, L. Shang, R. Shi, X. Kang, G. I. N. Waterhouse, L.-Z. Wu, C.-H. Tung, T. Zhang, *Adv. Energy Mater.* **2016**, *6*, 1502585.

[13] a) L. Yang, X. Zeng, D. Wang, D. Cao, *Energy Storage Mater.* **2018**, *12*, 277; b) Y. Li, M. Gong, Y. Liang, J. Feng, J.-E. Kim, H. Wang,

ADVANCED
SCIENCE NEWS
www.advancedsciencenews.com

ADVANCED
MATERIALS
www.advmat.de

G. Hong, B. Zhang, H. Dai, *Nat. Commun.* **2013**, *4*, 1805; c) Y. Zhang, H. Jiang, Y. Lin, H. Liu, Q. He, C. Wu, T. Duan, L. Song, *Adv. Mater. Interfaces* **2018**, *5*, 1800392.

[14] G.-L. Tian, Q. Zhang, B. Zhang, Y.-G. Jin, J.-Q. Huang, D. S. Su, F. Wei, *Adv. Funct. Mater.* **2014**, *24*, 5956.

[15] D. Yan, Y. Li, J. Huo, R. Chen, L. Dai, S. Wang, *Adv. Mater.* **2017**, *29*, 1606459.

[16] a) B.-Q. Li, S.-Y. Zhang, C. Tang, X. Cui, Q. Zhang, *Small* **2017**, *13*, 1700610; b) H. Li, S. Chen, H. Lin, X. Xu, H. Yang, L. Song, X. Wang, *Small* **2017**, *13*, 1701487.

[17] A. Wang, J. Li, T. Zhang, *Nat. Rev. Chem.* **2018**, *2*, 65.

[18] B. Qiao, A. Wang, X. Yang, L. F. Allard, Z. Jiang, Y. Cui, J. Liu, J. Li, T. Zhang, *Nat. Chem.* **2011**, *3*, 634.

[19] a) P. Liu, Y. Zhao, R. Qin, S. Mo, G. Chen, L. Gu, D. M. Chevrier, P. Zhang, Q. Guo, D. Zang, B. Wu, G. Fu, N. Zheng, *Science* **2016**, *352*, 797; b) C. Wang, H. Xie, S. Chen, B. Ge, D. Liu, C. Wu, W. Xu, W. Chu, G. Babu, P. M. Ajayan, L. Song, *Adv. Mater.* **2018**, *30*, 1802525.

[20] a) Z. Zhang, J. Sun, F. Wang, L. Dai, *Angew. Chem., Int. Ed.* **2018**, *57*, 9038; b) M. Zhang, Y.-G. Wang, W. Chen, J. Dong, L. Zheng, J. Luo, J. Wan, S. Tian, W.-C. Cheong, D. Wang, Y. Li, *J. Am. Chem. Soc.* **2017**, *139*, 10976; c) H. Fei, J. Dong, M. J. Arellano-Jimenez, G. Ye, N. D. Kim, E. L. G. Samuel, Z. Peng, Z. Zhu, F. Qin, J. Bao, M. J. Yacaman, P. M. Ajayan, D. Chen, J. M. Tour, *Nat. Commun.* **2015**, *6*, 8668; d) J. Wang, L. Gan, W. Zhang, Y. Peng, H. Yu, Q. Yan, X. Xia, X. Wang, *Sci. Adv.* **2018**, *4*, eaap7970.

[21] H. J. Qiu, Y. Ito, W. Cong, Y. Tan, P. Liu, A. Hirata, T. Fujita, Z. Tang, M. Chen, *Angew. Chem., Int. Ed.* **2015**, *54*, 14031.

[22] H. Fei, J. Dong, Y. Feng, C. S. Allen, C. Wan, B. Volosskiy, M. Li, Z. Zhao, Y. Wang, H. Sun, P. An, W. Chen, Z. Guo, C. Lee, D. Chen, I. Shakir, M. Liu, T. Hu, Y. Li, A. I. Kirkland, X. Duan, Y. Huang, *Nat. Catal.* **2018**, *1*, 63.

[23] Y. Chen, S. Ji, Y. Wang, J. Dong, W. Chen, Z. Li, R. Shen, L. Zheng, Z. Zhuang, D. Wang, Y. Li, *Angew. Chem., Int. Ed.* **2017**, *56*, 6937.

[24] a) Y. Han, Z. Wang, R. Xu, W. Zhang, W. Chen, L. Zheng, J. Zhang, J. Luo, K. Wu, Y. Zhu, C. Chen, Q. Peng, Q. Liu, P. Hu, D. Wang, Y. Li, *Angew. Chem., Int. Ed.* **2018**, *57*, 11262; b) X. Wang, W. Chen, L. Zhang, T. Yao, W. Liu, Y. Lin, H. Ju, J. Dong, L. Zheng, W. Yan, X. Zheng, Z. Li, X. Wang, J. Yang, D. He, Y. Wang, Z. Deng, Y. Wu, Y. Li, *J. Am. Chem. Soc.* **2017**, *139*, 9419.

[25] C. Tang, B. Wang, H.-F. Wang, Q. Zhang, *Adv. Mater.* **2017**, *29*, 1703185.

[26] T. He, S. Chen, B. Ni, Y. Gong, Z. Wu, L. Song, L. Gu, W. Hu, X. Wang, *Angew. Chem., Int. Ed.* **2018**, *57*, 3493.

[27] N. Huang, P. Wang, D. Jiang, *Nat. Rev. Mater.* **2016**, *1*, 16068.

[28] A. P. Cote, H. M. El-Kaderi, H. Furukawa, J. R. Hunt, O. M. Yaghi, *J. Am. Chem. Soc.* **2007**, *129*, 12914.

[29] X. Chen, M. Addicoat, E. Jin, L. Zhai, H. Xu, N. Huang, Z. Guo, L. Liu, S. Irle, D. Jiang, *J. Am. Chem. Soc.* **2015**, *137*, 3241.

[30] a) Z.-S. Wu, L. Chen, J. Liu, K. Parvez, H. Liang, J. Shu, H. Sachdev, R. Graf, X. Feng, K. Muellen, *Adv. Mater.* **2014**, *26*, 1450; b) S. Brueller, H.-W. Liang, U. I. Kramm, J. W. Krumpfer, X. Feng, K. Muellen, *J. Mater. Chem. A* **2015**, *3*, 23799.

[31] B.-Q. Li, S.-Y. Zhang, B. Wang, Z.-J. Xia, C. Tang, Q. Zhang, *Energy Environ. Sci.* **2018**, *11*, 1723.

[32] J. Wang, X. Ge, Z. Liu, L. Thia, Y. Yan, W. Xiao, X. Wang, *J. Am. Chem. Soc.* **2017**, *139*, 1878.

[33] D. W. Thomas, A. E. Martell, *J. Am. Chem. Soc.* **1959**, *81*, 5111.

[34] S. Dubin, S. Gilje, K. Wang, V. C. Tung, K. Cha, A. S. Hall, J. Farrar, R. Varshneya, Y. Yang, R. B. Kaner, *ACS Nano* **2010**, *4*, 3845.

[35] B.-Q. Li, S.-Y. Zhang, L. Kong, H.-J. Peng, Q. Zhang, *Adv. Mater.* **2018**, *30*, 1707483.

[36] W. Liu, L. Zhang, W. Yan, X. Liu, X. Yang, S. Miao, W. Wang, A. Wang, T. Zhang, *Chem. Sci.* **2016**, *7*, 5758.

[37] Y. Han, Y.-G. Wang, W. Chen, R. Xu, L. Zheng, J. Zhang, J. Luo, R.-A. Shen, Y. Zhu, W.-C. Cheong, C. Chen, Q. Peng, D. Wang, Y. Li, *J. Am. Chem. Soc.* **2017**, *139*, 17269.

[38] a) C. Tang, H.-F. Wang, X. Chen, B.-Q. Li, T.-Z. Hou, B. Zhang, Q. Zhang, M.-M. Titirici, F. Wei, *Adv. Mater.* **2016**, *28*, 6845; b) Y. Gorlin, T. F. Jaramillo, *J. Am. Chem. Soc.* **2010**, *132*, 13612.

[39] a) P. Chen, T. Zhou, L. Xing, K. Xu, Y. Tong, H. Xie, L. Zhang, W. Yan, W. Chu, C. Wu, Y. Xie, *Angew. Chem., Int. Ed.* **2017**, *56*, 610; b) J. Wang, H. Wu, D. Gao, S. Miao, G. Wang, X. Bao, *Nano Energy* **2015**, *13*, 387; c) Y. Su, Y. Zhu, H. Jiang, J. Shen, X. Yang, W. Zou, J. Chen, C. Li, *Nanoscale* **2014**, *6*, 15080; d) J. Zhang, Z. Zhao, Z. Xia, L. Dai, *Nat. Nanotechnol.* **2015**, *10*, 444.

[40] J. Fu, Z. P. Cano, M. G. Park, A. Yu, M. Fowler, Z. Chen, *Adv. Mater.* **2017**, *29*, 1604685.

[41] H. B. Yang, J. Miao, S.-F. Hung, J. Chen, H. B. Tao, X. Wang, L. Zhang, R. Chen, J. Gao, H. M. Chen, L. Dai, B. Liu, *Sci. Adv.* **2016**, *2*, e1501122.